ARTICLE   OPEN

Check for updates

Corrosion behavior of TiZrHfBeCu(Ni) high-entropy bulk metallic glasses in 3.5 wt. % NaCl

Pan Gong [1,2✉], Dongliang Wang[1], Cheng Zhang[1], Ying Wang[3], Zahra Jamili-Shirvan[4], Kefu Yao[5] and Xinyun Wang[1✉]

The corrosion behavior of TiZrHfBeCu(Ni) high-entropy bulk metallic glasses (HE-BMGs) has been investigated. The TiZrHfBeCu(Ni) HE-BMGs exhibited high corrosion resistance in 3.5 wt. % NaCl solution because of accumulation of ZrO_2 and TiO_2 in the passive film. Ni promoted increases of the ZrO_2, TiO_2, and HfO_2 contents and a decrease of the BeO content, which improved the HE-BMG corrosion behavior. Compared with $Zr_{41.2}Ti_{13.8}Ni_{10}Cu_{12.5}Be_{22.5}$ BMG, the high-entropy effect of HE-BMGs can significantly reduce the atomic mobility, which inhibits outward migration of Cu, reduces the kinetics of the dissolution reaction, and inhibits inward erosion by Cl^-, thereby improving the corrosion performance.

INTRODUCTION

Bulk metallic glasses (BMGs) are characterized by long-range disordered and short-range ordered structures at the atomic scale[1], and they have a large elastic limit, good magnetic properties, and high corrosion resistance[2,3]. Similar to traditional crystalline alloys, most developed BMGs are based on a single principle element or dual principle elements, such as Zr-, Ti-, Fe-, Ca-, Pd-, Mg-, and CuZr-based BMGs. In 2004, Yeh et al.[4] proposed a concept for alloy composition design, where the alloy is composed of five or more major elements in equimolar ratio or nearly equimolar ratio and the concentration of each alloy element is 5–35 at. %. They defined this type of alloy as high-entropy alloys (HEAs), which can break through the primitive limitations of traditional alloys. The characteristics of the multiple principle elements in the HEAs determine that they have high mixing entropy, which helps to form a disordered solid-solution phase, and they have better mechanical and physical properties[5-7]. With development of HEAs, it has gradually been discovered that some HEAs form an amorphous structure while having high mixing entropy. In 2002, Inoue et al.[8] prepared a rod sample of the TiZrHfCuNi BMG with a diameter of 1.5 mm, which was the first reported HEA capable of forming an amorphous structure. Wang et al.[9] developed $Sr_{20}Ca_{20}Yb_{20}Mg_{20}Zn_{20}$, $Sr_{20}Ca_{20}Yb_{20}Mg_{20}Zn_{10}Cu_{10}$, and $Sr_{20}Ca_{20}Yb_{20}(Li_{0.55}Mg_{0.45})Zn_{20}$ BMGs with high mixing entropy in 2011. In 2014, they proposed the definition of HE-BMGs[10]: BMGs containing five or more elements with the same or similar atomic percentages. Compared with conventional BMGs, HE-BMGs have relatively high mixing entropies[11]. At present, the developed HE-BMG systems include TiZr(Hf)CuNiBe[12-15], GdTbDyAlCo(Ni)[16], ErDyCoAlGd[17], FeCoNi-MoPB[18], PdPtCuNiP[19], and FeCoNi (B, Si, P, C)[20]. HE-BMGs have the properties of both the structural characteristics of BMGs and the compositional characteristics of HEAs, which make HE-BMGs better than HEAs and BMGs in certain aspects. FeCoNi (B, Si, P, C) HE-BMGs[20-22] exhibit ultra-high yield strength of up to 3.6 GPa and good soft magnetic properties with low coercivity of 1.1 A m^{-1}, whereas the yield strength of the traditional CoCr-FeMnNi HEA is only 1.18 GPa and its coercivity is 5.7 kA m^{-1}[23,24].

GdTbDyAl (Fe, Co, Ni)[16] HE-BMGs show better magnetic refrigeration performance, which differs from HEAs. ErGdYAlCo HE-BMGs have higher viscosities and more sluggish crystallization behavior than conventional BMGs[25]. Compared with CaMgZn BMG (fracture strength of 354 MPa)[26], CaMgZnSrYb HE-BMGs have better mechanical properties (fracture strength of 382 MPa)[9]. TiZrHfBe-CuNi HE-BMG has higher creep resistance than HEAs and BMGs[27].

The corrosion behavior is one of the most important issues for structural and functional materials. BMGs do not contain the grain boundaries, dislocations, and second-class defects found in traditional alloys, and they also have better chemical uniformity, so they exhibit better corrosion behavior under normal circumstances[3,28]. At present, investigation of the corrosion behavior of BMGs is mostly focused on the alloying elements, heat treatment, and corrosion mechanism. For example, the corrosion current (I_{corr}) of $Fe_{68}Cr_8Mo_4Nb_4B_{16}$ BMG is between 10^{-6} and 10^{-7} A cm^{-2} in 3.5 wt. % NaCl[29]. Because the elements partition throughout crystallization, especially Cr, which leads to a non-homogeneous structure that preferentially triggers and holds pitting corrosion, the corrosion current is much lower than that of the crystallized alloy (10^{-4}–10^{-5} A cm^{-2}). Yu et al.[3] investigated the corrosion behavior of $(Zr_{58}Nb_3Cu_{16}Ni_{13}Al_{10})_{100-x}Y_x$ ($x = 0$, 0.5, 2.5 at. %) BMGs in 0.5 mol L^{-1} H$_2$SO$_4$. They found that addition of Y improves the electrochemical homogeneity of the Zr-based alloys, but it also facilitates dissolution of Cu, resulting in a slight deterioration of the corrosion behavior. Research on the corrosion behavior of HEAs has focused on plastic deformation, heat treatment, and alloying elements. Luo et al.[30] investigated the corrosion behavior of the CoCrFeMnNi HEA in 0.1 M H$_2$SO$_4$. Compared with 304 L stainless steel, which does not show obvious selective dissolution, I_{corr} increased from 10^{-5} to 10^{-4} A cm^{-2}. Shi et al.[31] investigated the Al$_x$CoCrFeNi HEA in 3.5 wt. % NaCl solution with addition of Al and the effect of heat treatment on the corrosion behavior. With addition of Al, the phase structure changed. They found that the structural differences and chemical separation led to deterioration of the corrosion behavior and 1250 °C heat treatment simplified the microstructure and reduced elemental segregation, which improved the corrosion behavior of

[1]State Key Laboratory of Materials Processing and Die & Mould Technology, School of Materials Science and Engineering, Huazhong University of Science and Technology, 430074 Wuhan, China. [2]Research Institue of Huazhong University of Science and Technology in Shenzhen, 518057 Shenzhen, China. [3]School of Mechanical Engineering, Wuhan Polytechnic University, 430000 Wuhan, China. [4]Esfarayen University of Technology, Esfarayen, North Khorasan, Iran. [5]School of Materials Science and Engineering, Tsinghua University, 100084 Beijing, China. ✉email: pangong@hust.edu.cn; wangxy_hust@hust.edu.cn

the alloy. However, there have been relatively few studies on the corrosion behavior with both the high-entropy effect and an amorphous structure, and these need to be further investigated.

HE-BMGs have the characteristics of both the high-entropy effect and a disordered atomic arrangement, and they are a good model material for studying corrosion behavior. However, the development history of HE-BMGs is so short that there are few systematic studies on corrosion resistance, and only focus on the measurement of electrochemical parameters[32]. Therefore, it is necessary to conduct systematic and in-depth research on corrosion resistance.

Among HE-BMGs, TiZrHfBeCu(Ni) is a typical HE-BMG system that has good glass-forming ability (up to 30 mm)[15], high fracture strength (2000 MPa)[11], and good room-temperature creep resistance[27]. Therefore, in this study, we investigated the corrosion behavior of $Ti_{20}Zr_{20}Hf_{20}Be_{20}Cu_{20}$ (TC), $Ti_{20}Zr_{20}Hf_{20}Be_{20}Cu_{10}Ni_{10}$ (TCN), and $Ti_{20}Zr_{20}Hf_{20}Be_{20}Ni_{20}$ (TN) HE-BMGs in 3.5 wt. % NaCl. Furthermore, on the one hand, $Zr_{41.2}Ti_{13.8}Ni_{10}Cu_{12.5}Be_{22.5}$ (Vit1) BMG[33] has great academic significance and commercial value, so many scientific researches use Vit1 as a model material. On the other hand, the design of high-entropy bulk metallic glasses (HE-BMGs) was based on the principle of substitution of similar components: in TiZrHfBeCu(Ni) alloys, Ti, Zr, and Hf can be divided into a class of elements, and the atomic proportion is 60 at. %. Cu and Ni are one type, and the atomic ratio is 20 at. %. Be is one type, and the atomic ratio is 20 at. %. The Zr and Ti atoms in the composition of Vit1 are 55 at. %, the proportion of Cu and Ni is 22.5 at. %, and the proportion of Be is 22.5 at.%. So the atomic percentages of TiZrHfBeCu(Ni) are very close with Vit1, which are very suitable for performance comparison with Vit1. Therefore, we adopt TiZrHfBeCu(Ni) as the research object.

In conclusion, this thesis systematically studies the corrosion resistance of the specified alloy. And in this paper, the composition and the high-entropy effect on the corrosion behavior of HE-BMGs were investigated. The micro-corrosion mechanism of HE-BMGs is then proposed, which will provide a theoretical basis for development and application of HE-BMGs.

RESULTS AND DISCUSSION

Amorphous structures and dynamic mechanical analysis

The XRD patterns of the four samples are shown in Fig. 1(a). The XRD patterns all consisted of only a broad diffraction peak without any sharp Bragg peaks, indicating that the four samples were all amorphous structures.

The glass-transition temperatures (T_g) and onset crystallization temperatures (T_x) of the four samples showed the order Vit1 < TC < TCN < TN (Fig. 1(b)). The HE-BMGs had higher glass-transition temperatures than Vit1. This shows that the special properties of the HE-BMGs improved the thermal stability of the amorphous phase. Compared with Vit1, the HE-BMGs also had larger atomic configuration densities[34].

To further compare the effect of the high-entropy effect on the alloys at the atomic scale, dynamic mechanical analysis (DMA) was performed to study the atomic mobility of the samples. For viscoelastic materials, the flexural modulus can be expressed as

$$E = \sigma/\varepsilon = E' + iE'' \tag{1}$$

where the storage modulus E' represents the elastic response and the loss modulus E'' corresponds to the viscoelastic components[35]. The changes of the normalized storage modulus (E'/E_u) or loss factor (tan δ) of the as-cast samples with temperature are shown in Fig. 1(d). E_u represents the unrelaxed modulus at ambient temperature, and the relationship between the phase lag δ and the modulus can be expressed as the loss factor tan δ, which is related to the atomic mobility[36]. It is worth noting that tan δ reaches its maximum value at intermediate temperatures. This stage is considered to be related to the main α relaxation, which is related to the cooperative movements of the atoms inside the metals. Related studies have shown that the atomic mobility can be evaluated by the value of the loss factor tan δ. Qiao et al.[37] used DMA to analyze structure relaxation, plastic deformation, and crystal-phase formation in $Ti_{40}Zr_{25}Ni_8Cu_9Be_{18}$, which reduced the atomic mobility of the material, and the atomic mobility and tan δ showed a positive correlation. The tan δ value of Vit1 was lower than those of the studied HE-BMGs, which showed that the atomic mobilities of the HE-BMGs were significantly lower than that of the traditional BMGs owing to the existence of sluggish diffusion.
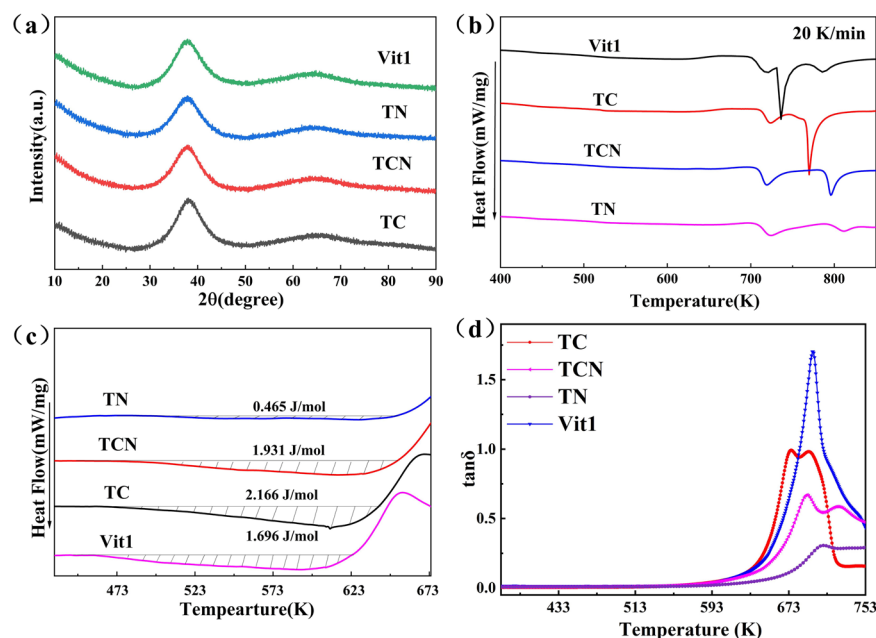

Fig. 1 The structures and dynamic mechanical analysis results of the samples. a XRD spectra, **b** DSC curves, **c** relaxation enthalpies, and **d** loss factors (tan $\delta = E'/E''$) with a fixed frequency of 1 Hz and a constant heating rate of 5 K/min.
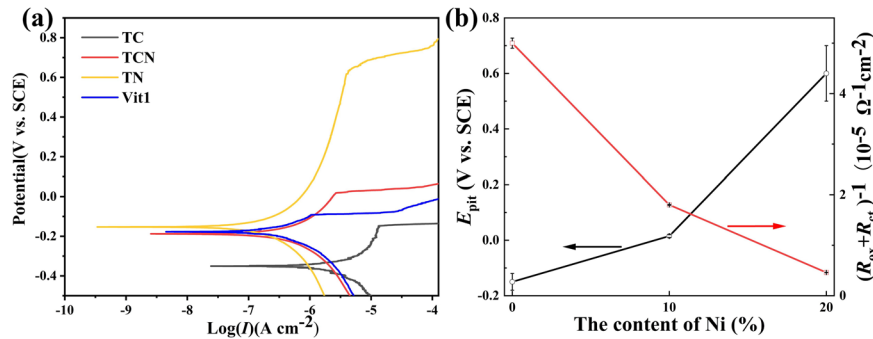
Fig. 2 Potentiodynamic polarization test results of the four samples in 3.5 wt. % NaCl at 298 K. a Polarization curves (**b**) Corrosion resistance (in terms of the pitting potential and $(R_{ox} + R_{ct})^{-1}$) as a function of the Ni content.

Table 1. Electrochemical parameters of the polarization curves of the four samples in 3.5 wt. % NaCl at 298 K.

Samples	E_{corr} (V)	i_{corr} (μA cm^{-2})	E_{pit} (V)	E_{pit}-E_{corr} (V)
Vit1	-0.26 ± 0.03	1.67 ± 0.10	-0.064 ± 0.01	0.086
TC	-0.38 ± 0.03	7.25 ± 0.05	-0.15 ± 0.03	0.20
TCN	-0.23 ± 0.02	0.92 ± 0.10	0.015 ± 0.01	0.21
TN	-0.16 ± 0.02	0.40 ± 0.10	0.60 ± 0.10	0.82

Electrochemical properties of the samples

The potentiodynamic polarization curves of the as-cast HE-BMGs and Vit1 in 3.5 wt. % NaCl at 298 K are shown in Fig. 2. The corrosion behavior of all of the alloys in NaCl showed common characteristics. (1) A short passivation region can be observed in the anodic polarization zone before pitting corrosion occurred. (2) All of the alloys showed obvious pitting corrosion. Through analysis of the potentiodynamic polarization curves, the corrosion potential (E_{corr}), corrosion current density (i_{corr}), and pitting potential (E_{pit}) are summarized in Table 1. E_{pit} represents the critical state for nucleation of pitting, and it has been widely used as a electrochemical parameter to estimate corrosion behavior[38]. From Table 1, the different alloys had significantly different pitting potentials, indicating that the stability and protective ability of the passive films showed considerable diversity. The pitting potential of the HE-BMGs as a function of the Ni content is shown in Fig. 2(b), based on the curves in Fig. 2(a). Therefore, the addition of elements affected the corrosion behavior of the HE-BMG. When Ni replaced Cu in the TC alloy, i_{corr} increased from 7.25×10^{-6} A cm^{-2} (TC) to 0.40×10^{-6} A cm^{-2} (TN), E_{pit} increased from -0.15 V$_{SCE}$ (TC) to 0.60 V$_{SCE}$ (TN), and the passivation region E_{pit}-E_{corr} increased from 0.2 V (TC) to 0.82 V (TN). Furthermore, for Vit1, $i_{corr} = 1.67 \times 10^{-6}$ A cm^{-2} and $E_{pit} = -0.064$ V$_{SCE}$, and for TCN, $i_{corr} = 1.67 \times 10^{-6}$ A cm^{-2} and $E_{pit} = -0.064$ V$_{SCE}$, so the corrosion resistance of Vit1 is between TC and TCN.

To evaluate the electronic properties and stabilities of the passive films, EIS measurements of the as-cast HE-BMGs and Vit1 were performed. The Nyquist and Bode plots of the four samples in 3.5 wt. % NaCl are shown in Fig. 3. Each Nyquist plot showed a single capacitive semicircle (Fig. 3(a)), which indicates that the corrosion process is controlled by the charge-transfer process[39]. However, each Nyquist plot had a different radius, and TN exhibited the largest impedance, which indicated that the interface had higher resistance data. From the Bode impedance plots in Fig. 3(b), the higher impedance in the low-frequency region indicated higher resistance to charge transfer. From the Bode impedance plots, TN may exhibit higher resistance to charge transfer. This suggests that the charge-transfer process was more difficult on the surface of TN, indicating that the passive film

formed on TN had high stability. This is consistent with the potentiodynamic polarization results and Nyquist plots.

To further analyze the impedance, the impedance results were fitted by the equivalent electric circuit (EEC) with two defined time constants shown in Fig. 3(c). In the EEC, R_s is the solution resistance, R_{ox} and R_{ct} are the resistance of the passive film and charge transfer, and CPE_{ox} and CPE_{ct} are the capacitance of the passive film formed on the surface and the double layer due to the electrochemical reaction at the solution/electrode interface. The CPE explains the non-ideal capacitance response because of the heterogeneous surface. The impedance CPE is given by[40]

$$Z(CPE) = Q_0^{-1}(j\omega)^{-n} \tag{2}$$

where Q_0 is a constant phase coefficient, $j = \sqrt{-1}$, ω is the angular frequency, and n is the dispersion index (0–1). The fitting results of the Nyquist plots are summarized in Table 2 The double layer capacitance (C_{dl}) can be evaluated by Brug's formula[40]:

$$C_{dl} = Q_1^{1/n}\left(R_S^{-1} + R_{ct}^{-1}\right)^{(n_1-1)/n_1} \tag{3}$$

The capacitance of the oxide film (C_{ox}) was calculated by the Hsu–Mansfeld equation[41]:

$$C_{ox} = Q_2(\omega_m'')^{(n_2-1)/n_2} \tag{4}$$

where ω_m'' is the frequency at which the imaginary part of the impedance has a maximum. The thickness of the oxide film can be calculated using the equation of a parallel-plate capacitor[42]:

$$C_{ox} = \frac{\varepsilon\varepsilon_0}{d} \tag{5}$$

where ε is the dielectric constant of the passive film, which is assumed to be 12.38, ε_0 is the vacuum permittivity ($\varepsilon_0 = 8.85 \times 10^{-14}$ F cm^{-1}), and d is the oxide thickness. The fitting parameters extracted from the EEC are summarized in Table 2. According to the fitting data in Table 2, the n_1 and n_2 values of all of the samples were <1, indicating that the non-ideal capacitive behavior of CPE was caused by the uneven current distribution because of the inhomogeneous surface, such as roughness and defects[43]. The C_{dl} values of the four samples showed the order TC > Vit1 > TCN > TN. A smaller C_{dl} value means that the corrosion area of the sample is smaller and the corrosion resistance is better. The C_{ox} values related to the thickness of the passive layer showed the order TC > Vit1 > TCN > TN, which means that the passive film formed on the TC sample with the smallest C_{ox} was thinner and more sensitive to erosion by Cl^{-}[44]. The total resistance ($R_{ox} + R_{ct}$) was chosen as the criterion for judging the corrosion resistance, and its change trend showed the order TC < Vit1 < TCN < TN. The decrease of the total resistance value is related to the decrease of the stability of the passive film and the increase of defects in the passive film. The TN sample showed the best corrosion resistance, which is consistent with the above research results, and the same
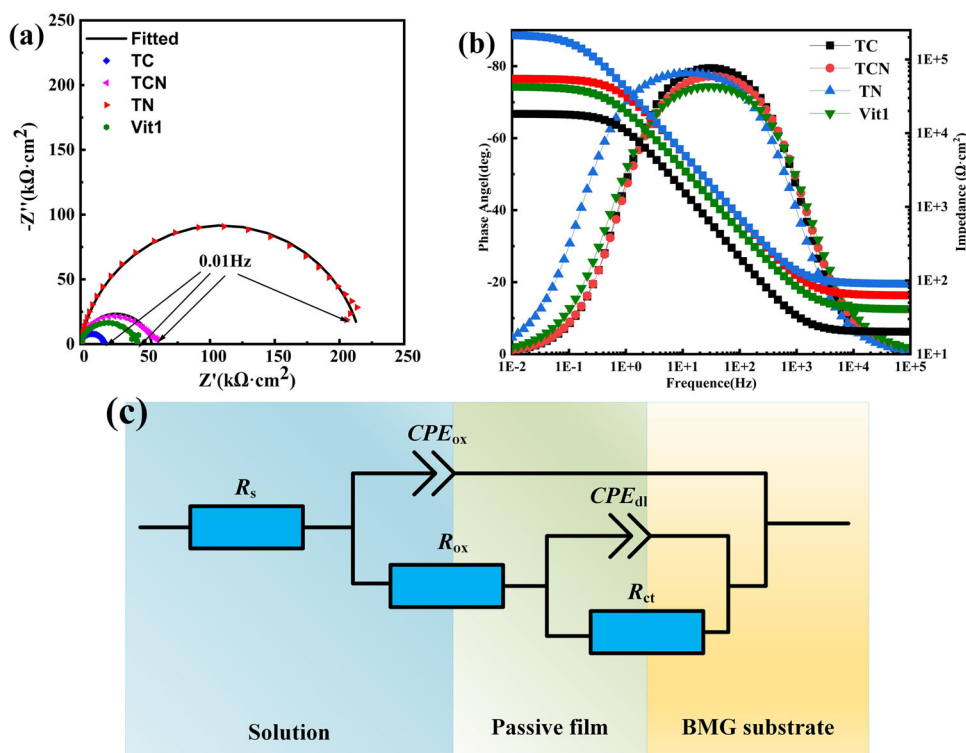
Fig. 3 EIS results of the samples under the OCP condition in 3.5 wt. % NaCl. a Nyquist, **b** Bode plots and **c** EEC used for fitting the EIS experimental data.

Table 2. Equivalent circuit fitting parameters for EIS of the samples in 3.5 wt. % NaCl solution under OCP conditions.

	R_s (Ω cm^2)	CPE_{dl}		R_{ct} (kΩ cm^2)	C_{dl} (μF cm^{-2})	CPE_{ox}		R_{ox} (Ω cm^2)	C_{ox} (μF cm^{-2})	d(nm)
		n_1 (0–1)	Q_1 (10^{-5} Ω^{-1} s^n cm^{-2})			n_2 (0–1)	Q_2 (10^{-6} Ω^{-1} s^n cm^{-2})			
Vit1	40.50 ± 0.38	0.86 ± 0.002	8.25 ± 0.011	42.90 ± 0.40	2.26 ± 0.08	0.87 ± 0.003	8.00 ± 0.007	14.08 ± 0.03	8.79 ± 0.07	1.75 ± 0.08
TC	20.13 ± 0.12	0.92 ± 0.002	1.16 ± 0.013	18.29 ± 0.11	6.19 ± 0.20	0.95 ± 0.002	9.23 ± 0.013	3.95 ± 0.01	9.31 ± 0.05	1.48 ± 0.05
TCN	62.66 ± 0.84	0.91 ± 0.004	0.44 ± 0.010	54.89 ± 0.71	1.78 ± 0.08	0.89 ± 0.002	4.49 ± 0.017	19.69 ± 0.01	4.58 ± 0.09	3.39 ± 0.08
TN	70.12 ± 0.62	0.89 ± 0.01	0.43 ± 0.004	217.04 ± 1.83	1.70 ± 0.05	0.90 ± 0.004	0.97 ± 0.006	23.54 ± 0.02	1.18 ± 0.06	9.29 ± 0.06

result can also be seen in Fig. 2(b), where the corrosion resistance gradually increased with increasing Ni content.

Pit morphology

To investigate the corrosion behavior of the alloys, SEM was performed to observe the pit morphology after the polarization test. Visible pits formed on the surfaces of the four samples. The pits of the samples were randomly distributed, but the microscopic morphology features were slightly different in Fig. 4.

For TC and Vit1, the pits were mainly circular extending toward the matrix, and there were obvious micro-cracks at the bottom, showing the characteristics of dealloying by electrochemical reaction. To further understand the element distribution of the pits, EDS were performed to scan the pits. Owing to selective dissolution of Zr and Ti, Cu was distributed along the pits (Fig. 4(c) and (l)). There were obvious Cu-rich, Ti-poor, and Zr-poor areas inside the pits, and the element distribution was not homogeneous, so the passive film formed on the surface was relatively weak and prone to corrosion. For the TCN and TN samples, the pits mainly showed a long and narrow shape extending toward the matrix, and dense microscopic cavities formed at the bottom of

the pits. The element distribution of the TN sample is shown in Fig. 4(j). The elements were evenly distributed on the surface.

Characteristics of the passive films

The corrosion behavior of an alloy is closely related to the structure and performance of the passive film. To further explore the corrosion behavior, Mott–Schottky (M–S) analysis and XPS were performed to investigate the characteristics of the passive films.

To further understand the electronic properties of the passive films, M–S analysis of the passive films formed on the surfaces of the high-entropy amorphous alloys and Vit1 alloy after soaking in NaCl solution for 3 h was performed. According to M–S theory, the relationship between the capacitance (C) of an n-type semiconductor pair and the applied potential can be described by the following equations[45]:

$$\frac{1}{C^2} = \frac{2}{N_D e \varepsilon \varepsilon_0}\left(E - E_{FB} - \frac{KT}{e}\right) \tag{6}$$

$$\frac{1}{C^2} = \frac{2}{N_A e \varepsilon \varepsilon_0}\left(E - E_{FB} - \frac{KT}{e}\right) \tag{7}$$
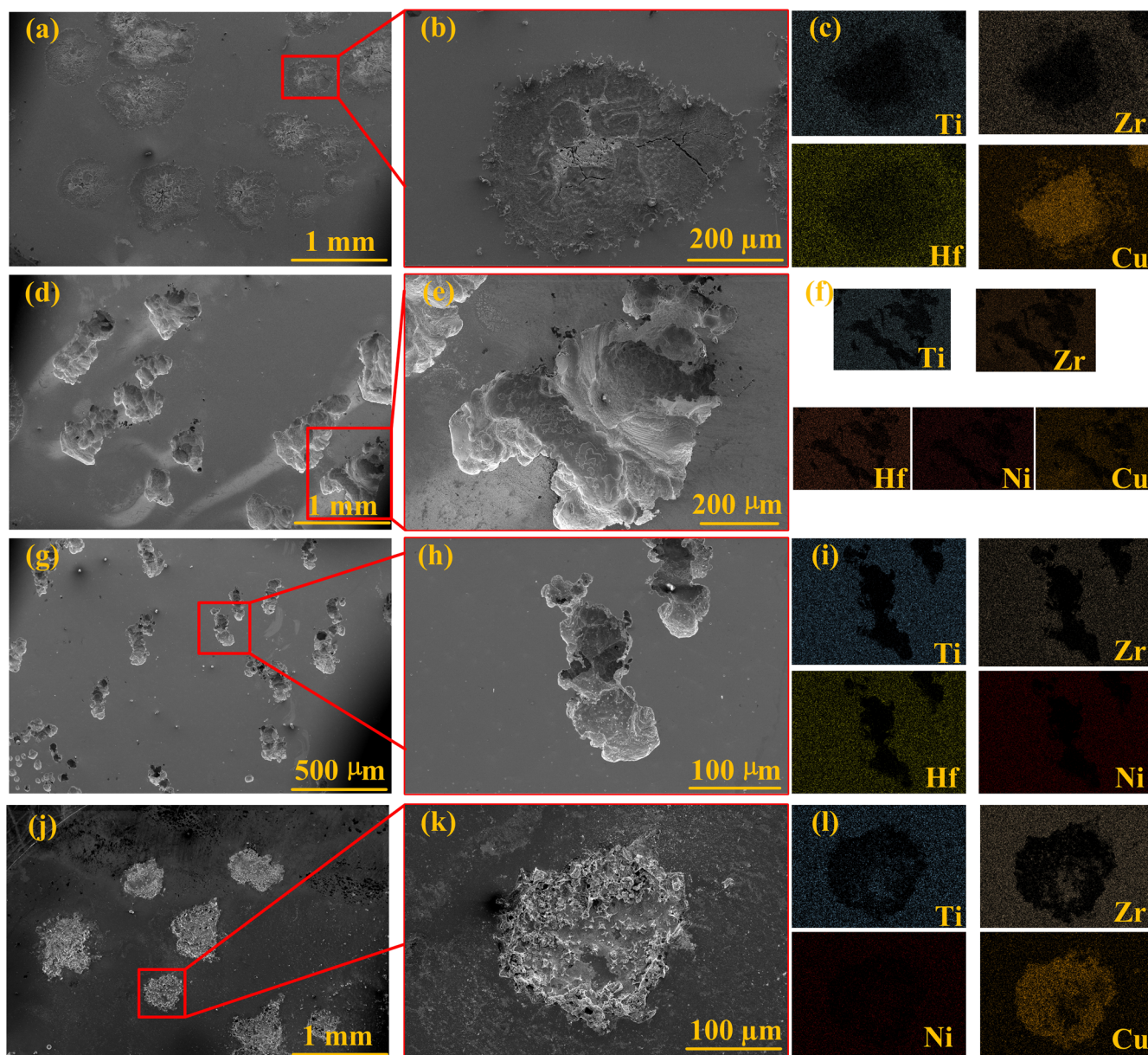
Fig. 4 The backscattered electron (BSE) image of the pit morphologies of the four samples. The SEM observations were performed immediately after the potentiodynamic polarization measurements in 3.5 wt. % NaCl solution. **a** TC sample, **b** magnified image of the area marked by the red square in **a**, and **c** EDS element mapping of the test area corresponding to **b**. **d** TCN sample, **e** magnified image of the area marked by the red square in **d**, and **f** EDS element mapping of the test area corresponding to **e**. **g** TN sample, (**h**) magnified image of the area marked by the red square in **g**, and **i** EDS element mapping of the test area corresponding to **h**. **j** Vit1 sample, **k** magnified image of the area marked by the red square in **j**, and **l** EDS element mapping of the test area corresponding to **k**.

where ε is the dielectric constant of the passive film (here, $\varepsilon = 12.38$), ε_0 is the vacuum permittivity constant ($\varepsilon_0 = 8.854 \times 10^{-14}$ F cm^{-1}), e is the elementary charge (1.602×10^{-19} C), N_D is the donor density of the n-type semiconductor, E_{FB} is the flat-band potential, K is the Boltzmann constant ($K = 8.16 \times 10^{-5}$ eV K^{-1}), and T is the absolute temperature (K)[46].

The M–S plots of the passive films obtained after immersing the samples in NaCl for 3 h are shown in Fig. 5(a). All of the specimens showed a linear region with a positive slope, indicating that the passive films were n-type semiconductors (i.e., oxygen vacancy doping type). The N_D values for TC, TCN, TN, and Vit1 were 4.56×10^{21}, 0.87×10^{21}, 0.34×10^{21}, and 3.97×10^{21} cm^{-3},

respectively. A higher N_D means that the passive film contains more oxygen vacancies (V_o) and it is easier for solution ions to adsorb, thereby causing the passive film to become unstable and the corrosion behavior to deteriorate[47]. Therefore, the change trend of N_D from the M–S plots is consistent with the corrosion behavior trend of the samples mentioned above. In addition, the flat-band potential E_{FB} can be obtained by M–S plot fitting[48]. The E_{FB} values for TC, TCN, TN, and Vit1 were -1.71, -1.212, -0.77, and -1.28 V vs. SCE, respectively. A positive shift of E_{FB} means that the energy barrier is larger and electron transfer is more difficult, so the stability of the passive film is improved[44].

To investigate the passivation behavior, XPS was performed to analyze the chemical compositions of the passive films on the
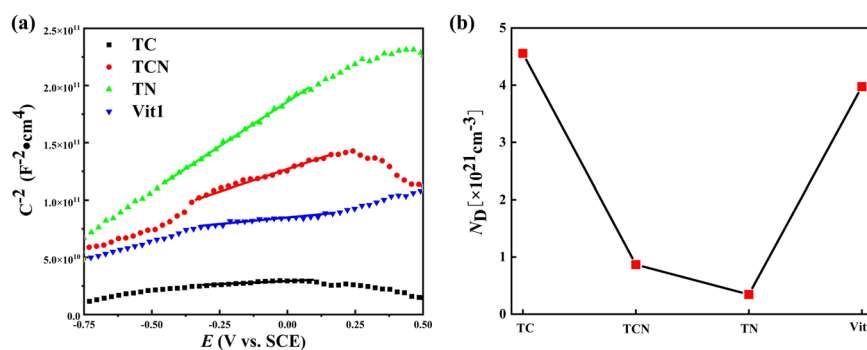
Fig. 5 M–S results of the samples after immersion in 3.5 wt. % NaCl for 3 h at 298 K. a M–S curves (**b**) Donor densities (N_D) in the passive films.

outermost surfaces after immersion in NaCl solution for 2 days. The XPS spectra of Ti 2p, Zr 3d, Hf 4f, and Be 1s distributed on the outermost surfaces of the alloys are shown in Figs. 6 and 7. For all of the samples, Ti, Zr, Hf, and Be exhibited very similar elemental valences, and the types of elemental valence showed no distinct differences. The Ti 2p spectra were composed of $2p_{1/2}$ peaks (464.4 eV) and $2p_{3/2}$ peaks (458.6 eV) of Ti^{4+}, and $2p_{1/2}$ peaks (458.9 eV) and $2p_{3/2}$ peaks (452.3 eV) of Ti^0. The Zr 3d spectra were composed of $3d_{3/2}$ peaks (184.8 eV) and $3d_{5/2}$ peaks (182.4 eV) of Zr^{4+}, and $3d_{3/2}$ peaks (180.9 eV) and $3d_{5/2}$ peaks (178.5 eV) of Zr^0. The Hf 4f spectra were composed of $4f_{5/2}$ peaks (18.7 eV) and $4f_{7/2}$ peaks (17.0 eV) of Hf^{4+}. The Be 1s spectra were mainly composed of Be^{2+} 1s peaks. The O 1s is mainly composed of H_2O, OH^- and O^{2-}, and the corresponding binding energies are 532.4 eV, 531.4 eV and 530.5 eV respectively[49,50].

Ti and Zr in the alloy can be easily oxidized to stable TiO_2 and ZrO_2 in a neutral or oxidizing environment[51]. The highly chemically stable TiO_2 and ZrO_2 contribute to formation of a protective passive film, thereby delaying the occurrence of corrosion[51]. However, the alloying elements will affect the contents and stabilities of the oxides, especially for replacement of Cu with Ni. An increase of Ti^{4+}, Zr^{4+}, or Hf^{4+} is accompanied by a decrease of Cu^{2+} and Be^{2+}. To a certain extent, this indicates that the alloying elements will affect the contents of the other elements and the characteristics of the passive film.

The corrosion behavior and passivation behavior of metals are closely related to the characteristics of the alloying elements. Therefore, to further investigate the influence of Cu and Ni on the corrosion behavior and passive film, Ar ions were used to etch the surfaces of the samples for 240 s after immersion, and the samples after etching were analyzed by XPS. The XPS spectra of Cu and Ni on the surfaces and underlying surfaces of the samples are shown in Fig. 8; this helps to clarify the origin of the differences. The results showed that there were large differences in the distributions and contents of the elements on the surfaces and underlying surfaces of the four samples. (1) For the samples containing Cu, Cu^{2+} and Cu^0 were detected on the surface and underlying surface. The Cu element was mainly in the form of Cu^{2+}, but the content of Cu^0 significantly increased in the underlying surface. (2) For the sample containing Ni, the surface of the sample contained almost no Ni, while Ni^{2+} and Ni^0 were detected in the underlying surface, and Ni^0 was dominant. Combined with related studies, the presence of Cu in the sample will lead to deterioration of the corrosion behavior, and addition of Ni can improve the corrosion behavior in NaCl solution. However, from XPS analysis, the passive films did not contain much Ni.

To further investigate the distributions of the elements and the stabilities of the passive films, according to the integrated intensities of the XPS spectra, the relative concentrations of the cations are summarized in Fig. 9. When Ni replaced Cu, from TC to TN, the Ti element content increased from 7.37 to 24.55%, the Zr

element content increased from 11.69 to 31.69%, and the Hf element content increased from 11.74 to 38.55%, but the Be content decreased from 65.04 to 5.22%. The changes in the contents of the alloying elements Cu and Ni mainly caused the changes in the other elements in the passive film, which may be the main reason for the difference in the corrosion behavior.

To further investigate the variation in the passive film thickness and analyze the roles of Cu and Ni in the passivating process and passive film, we directly observed the passive films of the TC and TN samples. Cross-sectional TEM images and the element distributions of the samples are shown in Fig. 10. The passive film generated by the TC sample (3 nm) at the OCP for 3600 s was thinner than that of the TN sample (10 nm), indicating that the TN sample also had higher corrosion resistance, which is similar to the electrochemical test results. In addition, the element distribution showed that the passive film of the TC sample contained large enrichment of the Cu element. However, for the TN sample, there was almost no Ni in the passive film, which may be caused by preferential dissolution of Ni, which is consistent with the XPS measurement.

Through analysis of the above results, the following interesting results were obtained. (1) Addition of Ni affected the composition and content of the passive film, thereby affecting the corrosion behavior. (2) Compared with the common Vit1, there were obvious differences in the corrosion behavior. In the next section, we will focus on the following issues: (1) the mechanism of the effect of Ni on the corrosion behavior of HE-BMGs, (2) the advantages of HE-BMGs owing to the special composition characteristics compared with the traditional Vit1, and (3) the corrosion mechanism of HE-BMGs.

Corrosion behavior and mechanism of the HE-BMGs

The corrosion behavior of an alloy is usually related to the passive film on its surface. In this study, the corrosion behavior of the HE-BMGs mainly improved by adjusting the material composition, and the composition directly affected the passive film composition. Thus, this improvement can be considered from the perspective of the passive film composition. The passive films of the HE-BMGs mainly consisted of ionic components (Ti^{4+}, Zr^{4+}, Hf^{4+}, Be^{2+}, and Cu^{2+}) and metallic components (Ti^0, Zr^0, Be^0, and Cu^0), and the formed film containing highly stable TiO_2 and ZrO_2 was highly protective. However, the specific situation may be slightly different. On the one hand, with addition of Ni, the passive film on the outermost surfaces was rich in Ti, Zr, and Hf with a large decrease of the Be content (Fig. 6). On the other hand, the passive film on the outermost surfaces contained little Ni (Figs. 8 and 10). According to the formula (8)–formula (13), the standard
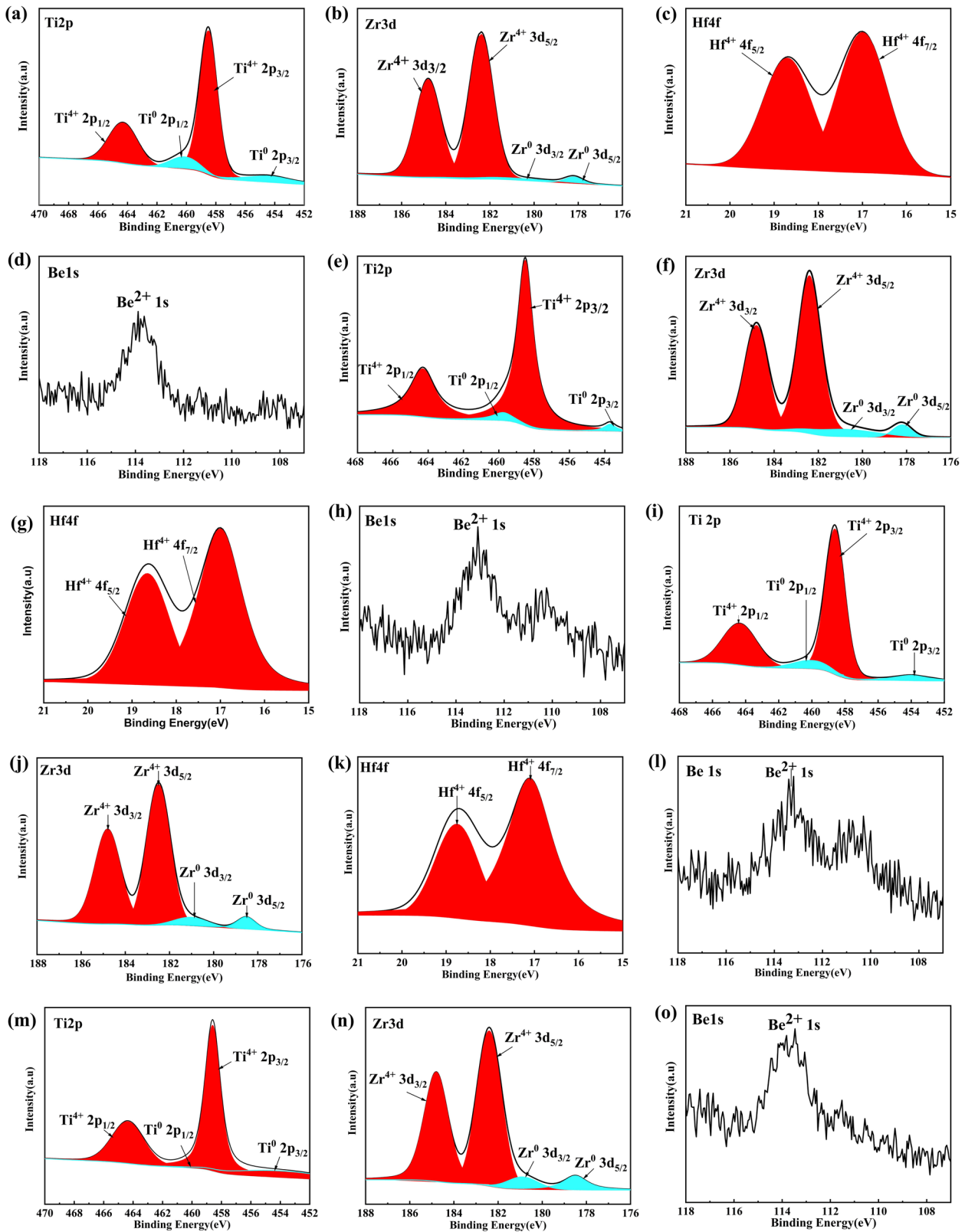
Fig. 6   XPS spectra of the outermost surfaces (without Ar-ion etching) of the samples after immersion in NaCl solution for 2 days. a–d TC sample, **e–h** TCN sample, **i–l** TN sample, and **m–o** Vit1 sample.
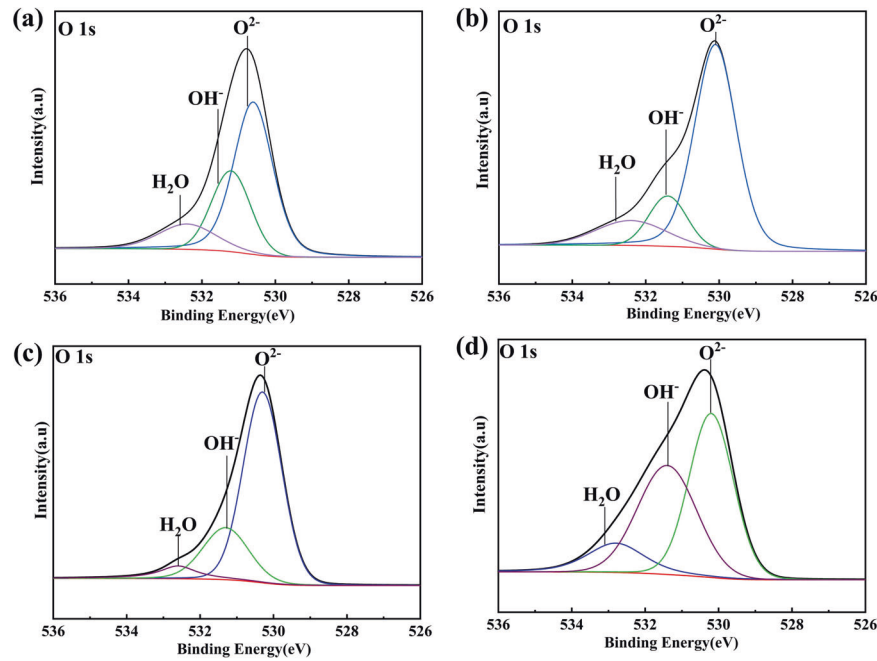
Fig. 7 The O 1s spectra for different alloys. a TC, **b** TCN, **c** TN, and **d** Vit1.

electrode potentials of Ti, Zr, Hf, Be, Cu, and Ni are:

$$Ti = Ti^{4+} + 4e^- - 1.902 \, V/SCE \tag{8}$$

$$Zr = Zr^{4+} + 4e^- - 1.692 \, V/SCE \tag{9}$$

$$Hf = Hf^{4+} + 4e^- - 1.792 \, V/SCE \tag{10}$$

$$Be = Be^{2+} + 2e^- - 2.089 \, V/SCE \tag{11}$$

$$Cu = Cu^{2+} + 2e^- \, 0.098 \, V/SCE \tag{12}$$

$$Ni = Ni^{2+} + 2e^- - 0.492 \, V/SCE \tag{13}$$

According to the standard electrode potentials[52], the electrode potentials of these elements are lower than the tested E_{corr}, except for Cu, indicating that these elements probably spontaneously passivate to form a protective passive film or preferentially dissolve to form free ions (e.g., Ni). In addition, according to the element thermodynamics, for Ti, Zr, Be, and Hf in 3.5 wt. % NaCl solution (pH = 6.4), their Pourbaix diagrams show that TiO_2, ZrO_2, HfO_2, and BeO are oxidized at a given potential and pH value[3,52,53]. This is consistent with the passive film composition obtained by XPS measurement, but it is completely opposite to Cu and Ni[53]. Under this condition, Ni is considered to preferentially dissolve[54]. Therefore, the absence of the Ni component in the passive film is caused by preferential dissolution of Ni[53].

From the above EIS and M–S test results, the traditional point defect model (PDM) can be used to describe corrosion of the HE-BMGs in NaCl solution to explain the corrosion mechanism of the alloy from the perspective of kinetics[55,56]. Reaction (14) shows that cation vacancies are generated from the metal cations Ti, Zr, Be, Hf, Ni, and Cu at the film/solution interface and migrate to the matrix/film interface. Through Reaction (15) at the matrix/film interface, the cation vacancies are then consumed by combining with metal atoms, which represents the dissolution process of the passive film. Reactions (16) and (17) indicate that the anion vacancies are generated at the matrix/film interface and consumed at the film/solution interface, which indicates the formation process of the passive film. Reaction (18), which is

related to dissolution, eventually causes destruction of the film.

$$M_M \rightarrow M_{aq}^{\delta+} + V_M^n + (\delta - n)e' \tag{14}$$

$$m + V_M^n \rightarrow M_M + V_m + ne' \tag{15}$$

$$m \rightarrow M_M + (n/2)V_O^- + ne' \tag{16}$$

$$V_O^- + H_2O \rightarrow O_O + 2H^+ \tag{17}$$

$$MO_{n/2} + nH^+ \rightarrow M^{\delta+} + (n/2)H_2O + (\delta - n)e' \tag{18}$$
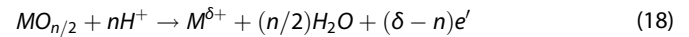
where M_M is a metal cation, m is a metal atom, O_O is an oxygen ion, V_M^n is a cation vacancy, and V_O^- is an anion vacancy. Based on analysis with the PDM, a schematic of the evolution of the passive film is shown in Fig. 11. According to the PDM model, formation of the passive film at the matrix/film interface and the dissolution process of the passive film at the film/solution interface will reach a dynamic equilibrium, which is determined by the transfer process of electrons, metal cations, and vacancies at the interface[55,56]. Formation of the passive film depends on the chemical stability of $MO_{n/2}$ in NaCl. However, when the obtained hydroxides are dense and stable, hydrolysis of the free metal cations also has a positive effect on formation and growth of the passive film[3]. Thus, the thermodynamic stability of the alloying elements in the electrolyte solution has an important influence on the characteristics of the passive film.

The difference of the corrosion behavior of the three HE-BMGs comes from the difference in the Ni and Cu contents. The effect of Ni on Ti- and Zr-based BMGs has been discussed in previous studies. Li et al.[57] studied the pitting corrosion kinetics of $Zr_{60}Ni_{25}Al_{15}$ and $Zr_{60}Cu_{25}Al_{15}$ in NaCl solution, and under their test conditions, the three components of $Zr_{60}Ni_{25}Al_{15}$ were all present in the active dissolution state. In contrast, for $Zr_{60}Cu_{25}Al_{15}$, only Zr and Al were in active dissolution, so the difference determines whether selective dissolution occurs. Gu et al.[53] studied the effects of Ni, Al, and Fe on the corrosion behavior of Ti–Zr–Be BMG, and Ni was not detected on the surface of the passive film. They suggested that Ni preferentially dissolves at the film/solution interface to promote formation of cation vacancies and promote formation of a stable passive film. This is consistent
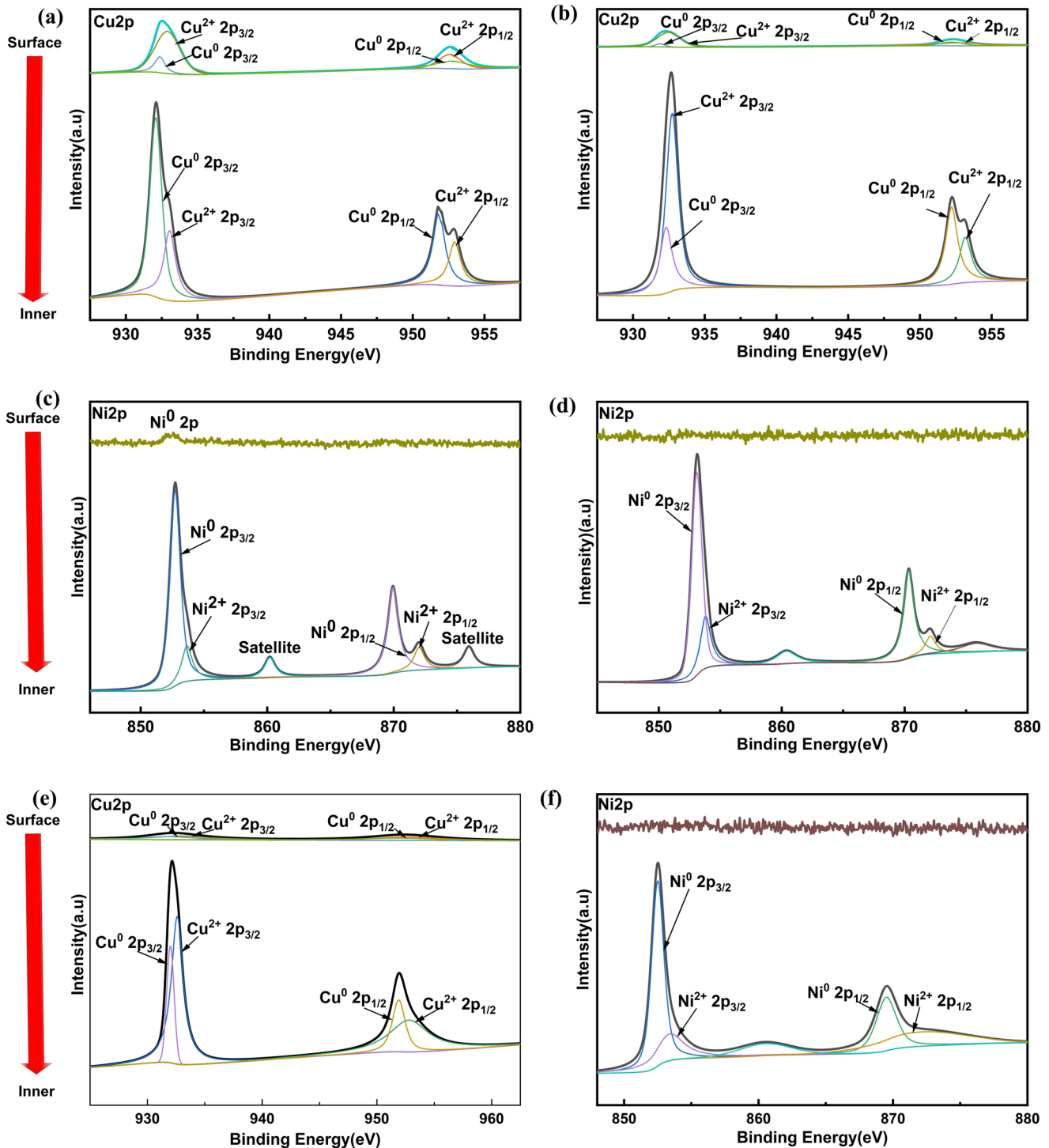
Fig. 8 Comparison of the XPS spectra of the alloying elements distributed on the outermost surfaces (without Ar-ion etching) and underlying surfaces (with Ar-ion etching, 240 s) after immersion in NaCl solution for 2 days. a Cu 2p spectra of the TC sample. **b** Cu 2p and **c** Ni 2p spectra of the TCN sample. **d** Ni 2p spectra of the TN sample. **e** Cu 2p and **f** Ni 2p spectra of the Vit1 sample.

with the result that Ni was not detected on the outermost surface by XPS (Fig. 8) and the TEM test (Fig. 10). According to the preferential dissolution process of Ni described in the above discussion, it will promote formation of cation vacancies and contribute to generation of metal cations, leading to enrichment of Ti and Zr in the passive film. Conversely, because addition of Ni will result in a decrease in the Be content in the passive film, while

Be and BeO will decrease the stability of the passive film in NaCl solution, the decrease of the Be content will improve the corrosion behavior[49,58].

According to the Pourbaix diagram, Cu can also form CuO in the passive film[52]. This is consistent with the XPS test results in Fig. 9, which means that Cu will fiercely compete with the other metals for the cation vacancies and bonding with oxygen. As shown in

Table 2, the R_p value reflects the migration resistance of the cation and anion vacancies[53]. In this HE-BMG system, the atomic radius of Cu (0.128 nm) is significantly smaller than those of the favorable elements Ti (0.146 nm), Zr (0.160 nm), and Hf (1.58 nm), which means that Cu more easily migrates and combines with oxygen. This enhances the competitiveness of Cu[53], but it also aggravates dissolution of Cu and deteriorates the corrosion behavior. With increasing Cu content, the R_p value gradually decreases, which indicates deterioration of the corrosion behavior.

Owing to the difference of the elements in the passive film, the affinity with Cl⁻ may also be different. For example, Ti, Zr, and Hf do not greatly react with Cl⁻ in neutral solution, and they can only form solid complexes, such as $ZrCl_4$, $TiCl_4$, and $HfCl_4$ complexes. By contrast, Cu readily reacts with Cl⁻, forming large amounts of soluble and insoluble precipitates and complexes[28]. Cu generates the chlorinated complex $CuCl^{2-}$[28], which directly results in instability and thinning of the passive film. In addition, previous studies have found that, especially during growth of the pits or when a passive film with a weaker material grows on physical defects and uneven areas[28], local selective dissolution of Ti and Zr makes the surface locally rich in Cu, which easily interacts with Cl⁻ to generate CuCl complexed species that easily hydrolyze in the pits to form Cu_2O, which is then deposited inside the pits[59]. However, the formed oxides are porous and have no protective effect, and dissolution of the material and spreading of the pits will continue, leading to an autocatalytic reaction with Cl⁻[60]. Schematic diagrams of the pitting mechanisms on the TC and TN samples during potentiodynamic polarization in 3.5 wt. % NaCl solution are shown in Fig. 12.

In summary, addition of Ni makes the atoms in the passive film rearrange and causes the film to be more stable and denser, thereby improving the corrosion behavior.

Influence of the high-entropy effect on corrosion behavior

Compared with the traditional Vit1 BMG, the HE-BMGs showed the obvious characteristic of the high-entropy effect. In this paper, we have discussed the advantages of HE-BMGs and the traditional BMG. Therefore, we compared the corrosion behavior of the TiZrHfBeCu(Ni) HE-BMGs and traditional Vit1 BMG in 3.5 wt. % NaCl solution in this section, and we then compared the influence of the high-entropy effect on the corrosion behavior.

We focus on the specific effect of the high-entropy effect on the corrosion resistance of the alloys. According to the Fig. 1(d) and the previous analysis, the corrosion behavior of the HE-BMGs also seemed to have a certain relationship with the sluggish diffusion. The existence of Ti and Zr is the main reason for passivation of the samples, and dissolution of Cu will cause dissolution of the passive film. Therefore, dissolution of Cu and passivation of Ti and Zr are in a competitive relationship[52,61]. From the DMA results, Vit1 showed higher atomic mobility, and all of the elements were more active than those of the HE-BMGs. In addition to inhibiting migration of the passivation elements, the high-entropy effect can also inhibit migration of Cu. For TC, the Cu and strong passivation element contents in the alloy were 20 and 40 at. %, respectively, and the change caused by the high-entropy effect was minimal because the Cu content was too high. For TCN, the alloy did not contain Cu, so the formed passive film was relatively stable. However, for Vit1 and TCN, the Cu/(Ti+Zr) ratios were (12.5 at. %)/(55 at. %) and (10 at. %)/(40 at. %), respectively, but the TCN corrosion behavior was better than that of Vit1. Contrary to the study of Tang et al.[35], this is because the proportion of Cu for TCN was higher than that for Vit1, and dissolution of Cu was dominant in the competitive
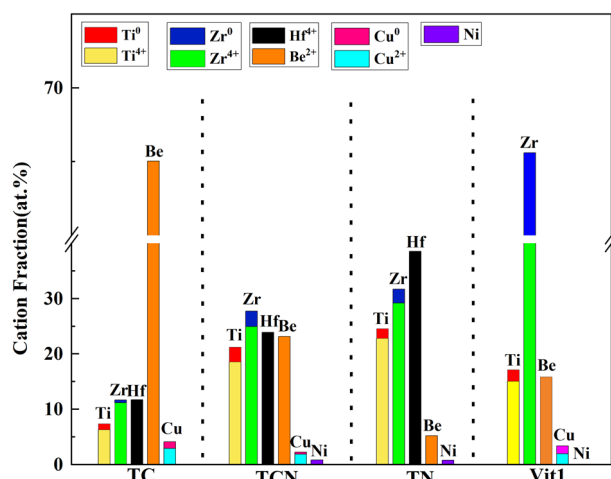
Fig. 9 Cation fractions in the passive films of different alloy samples obtained by XPS analysis. The adopted samples were immersed in 3.5 wt. % NaCl solution for 2 days.
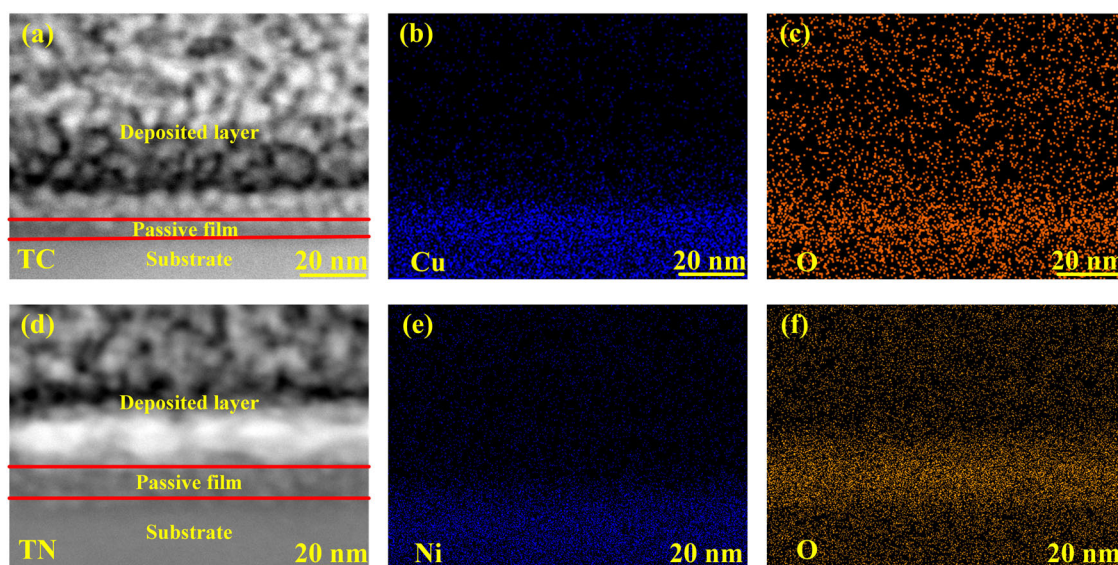
Fig. 10 TEM images of the passive films of the samples at the OCP in 3.5 wt. % NaCl solution for 3600 s. a TC sample. **b, c** EDS mapping images of the test area corresponding to **a. d** TN sample. **e, f** EDS mapping images of the test area corresponding to **d**.
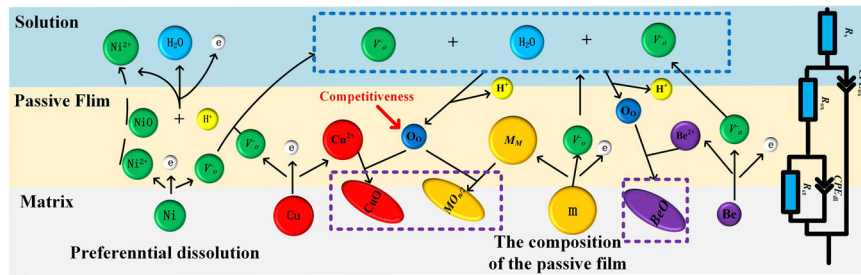
Fig. 11 Schematic illustration of passive film evolution for different alloy samples, which shows transition of the ions, electrons, and vacancies. For convenience, the far right subfigure shows the EEC used for fitting the EIS experimental data.
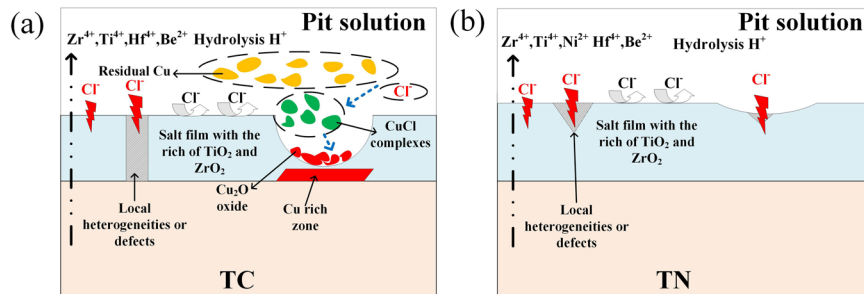

Fig. 12 Schematic diagrams of the pitting mechanisms for different alloys during potentiodynamic polarization in 3.5 wt. % NaCl solution. a TC and **b** TN.
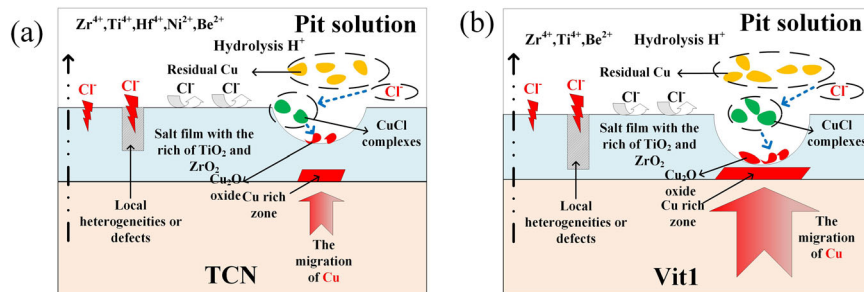

Fig. 13 Pitting mechanisms for different alloy samples during potentiodynamic polarization in 3.5 wt. % NaCl. a TCN and **b** Vit1.

process of formation of the passive film. Thus, the TCN alloy with a higher proportion of Cu can reduce the defects of the passive film, inhibit migration of Cu, and inhibit formation of cation vacancies through sluggish diffusion, thereby improving the corrosion behavior. The pitting mechanisms of the TCN and Vit1 samples during potentiodynamic polarization in 3.5 wt. % NaCl, especially the influence of the high-entropy effect on migration of Cu, which can easily explain the influence of the high-entropy effect on the corrosion behavior, are shown in Fig. 13. The dissolution process of the passive film involves migration of ions, electrons, and cation vacancies, and the mobility also affects the speed of the chemical reaction during the dissolution process. In the chemical reaction, the sluggish diffusion of the HE-BMGs leads to a decrease in the migration ability of the atoms, which in turn affects the chemical reaction process[62]. The existence of Cl⁻ is the main cause of pitting corrosion, and the existence of the high-entropy effect can inhibit diffusion of Cl⁻ to the passive film and matrix, thereby improving the corrosion behavior of the HE-BMGs. The cocktail effect of HE-BMGs also plays a positive role in the process of Ni replacing Cu.

Besides, in HE-BMGs, the cocktail effect is also emphasized majorly because at least five major elements are used to enhance

the properties of the materials. Specifically, various elements of the alloy have different properties, and the interaction between different elements makes the alloy show a composite effect, which emphasizes that some properties of the elements will eventually reflect the impact on macroscopic properties of the alloys[4,9,10,63,64]. In this paper, the cocktail effect of HE-BMGs also plays a positive role in the process of Ni replacing Cu.

Based on the above discussion, it can be inferred that the high corrosion resistance of the HE-BMGs is because of sluggish diffusion and the cocktail effect. That is, reduction of the atomic mobility caused by sluggish diffusion. First, it will inhibit diffusion of Cu in the HE-BMGs, thereby reducing formation of passive film defects and active dissolution of Cu. Second, it can reduce the dissolution reaction kinetics. Third, it can inhibit inward diffusion of Cl⁻. A series of electrochemical measurements confirmed this conclusion. Therefore, this study provides a mechanism to explain the corrosion behavior of HE-BMGs. However, attention needs to be paid to the corrosion mechanism in the actual corrosion process, which is more complicated. The high-entropy effect affects the corrosion behavior of alloys, but it does not play a key and decisive role[35], so it requires more extensive investigation.

METHODS

Preparation of samples

Metal ingots with purity of 99.9 wt. % were used as the raw materials. The master alloy ingots were prepared in a water-cooled copper mold crucible under an argon atmosphere using a high-vacuum arc induction arc melting apparatus. The ingots were re-melted five times to ensure chemical homogeneity. The HE-BMGs $Ti_{20}Zr_{20}Hf_{20}Be_{20}Cu_{20}$ (TC), $Ti_{20}Zr_{20}Hf_{20}Be_{20}Cu_{10}Ni_{10}$ (TCN), and $Ti_{20}Zr_{20}Hf_{20}Be_{20}Ni_{20}$ (TN), and the traditional BMG Vit1 $Zr_{41.2}Ti_{13.8}Ni_{10}Cu_{12.5}Be_{22.5}$ with diameter of 10 mm were prepared by copper mold casting.

Microstructure characterization

The microstructures of the as-cast samples were determined by X-ray diffraction (XRD-7000S, Cu-Kα radiation). The target material was a copper target, the scanning range (2θ) was 10°–90°, and the scanning speed was 15°/min. In this study, differential scanning calorimetry (DSC; NETZSCH STA 449C) was performed to analyze the thermodynamic parameters of the alloys. Under protection of an argon atmosphere, the alloy was heated from room temperature to 873 K at a heating rate of 20 K min^{-1}.

Dynamic mechanical analysis

To investigate the atomic mobility of the samples, dynamic mechanical analysis (DMA; TA DMA Q800) was performed under sinusoidal stress with a fixed frequency of 1 Hz to the sample and heating from room temperature to 873 K at a heating rate of 5 K min^{-1}. The size of the sample was 30 mm × 1 mm × 0.5 mm, and all of the tests were performed under an argon atmosphere to prevent oxidation.

Electrochemical characterization

For electrochemical measurement, the sample was cut to a diameter of 10 mm and a thickness of 5 mm. The surface of the sample was then polished with #400–#2000 silicon carbide sandpaper, polished with aluminum oxide, cleaned with acetone, ethanol, and de-ionized water, and finally dried in a drying oven for 3 h. All of the electrochemical measurements were performed with an electrochemical workstation (CS 310H, Corrtest) using a traditional three-electrode electrochemical system with platinum mesh as the auxiliary electrode, a saturated calomel electrode (SCE) as the reference electrode, and the sample as the working electrode. The electrolyte was 3.5 wt. % NaCl solution, and all of the electrochemical measurements were performed at room temperature. Before any of the electrochemical measurements were taken, the working electrode was reductively polarized at −1 V$_{SCE}$ for 3 min to clean the surface of the alloy. Before the electrochemical impedance spectroscopy (EIS) and potentiody-namic polarization tests, the sample was first immersed in the solution for 30 min to obtain a stable open-circuit potential (OCP). The frequency range of EIS was 0.01–10^5 Hz, and the tested voltage was the stable voltage value after 30 min of OCP stabilization. The voltage range of the potentiodynamic polariza-tion test was −0.5–1.2 V$_{SCE}$, and the scanning speed was 1 mV s^{-1}. To investigate the properties of the material's passive film, the sample was first soaked in the solution for 3 h, and then a Mott–Schottky test of the sample was performed at a frequency of 1000 Hz. To ensure the accuracy of the test, each electrochemical measurement was repeated three times.

Surface morphologies

Scanning electron microscopy (SEM; JSM-7600F) was performed to observe the surface morphology of the sample after EIS. The energy spectrum analyzer (EDS) that came with the instrument was used to perform element detection before and after corrosion.

Characterization of the passive film

X-ray photoelectron spectroscopy (XPS; Axis-ultra DLD-600W, SHIMADUS) was performed to obtain information about the passive film. The samples were immersed in the solution for 2 days to form a stable passive layer on the surface of the sample. Before the tests, absolute ethanol and de-ionized water were used to remove the residual corrosion liquid from the surface, and Ar$^+$ (30 s) was used to remove the surface contaminants. The charge correction method is corrected by the charge neutralization gun built into the gold conducting device, and the band pass energy is 40 eV. XPSPEAK software was used to fit the XPS curves of the XPS test results. The cross-sectional structure of the passive film formed by the sample at a stable OCP for 3600 s was observed by high-resolution transmission electron microscopy (HRTEM, FEI Titan G260-300). The TEM samples were fabricated by focused ion beam (FIB, FEI Helios 450S).

REFERENCES

1. Gu, J., Shao, Y. & Yao, K. The novel Ti-based metallic glass with excellent glass forming ability and an elastic constant dependent glass forming criterion. *Materialia* **8**, 100433 (2019).
2. Gu, J. et al. Centimeter-sized Ti-rich bulk metallic glasses with superior specific strength and corrosion resistance. *J. Non-Cryst. Solids* **512**, 206–210 (2019).
3. Yu, L. et al. Corrosion behavior of bulk ($Zr_{58}Nb_3Cu_{16}Ni_{13}Al_{10})_{100−x}Y_x$ (x = 0, 0.5, 2.5 at. %) metallic glasses in sulfuric acid. *Corros. Sci.* **150**, 42–53 (2019).
4. Yeh, J. W. et al. Nanostructured high-entropy alloys with multiple principal elements: novel alloy design concepts and outcomes. *Adv. Eng. Mater.* **6**, 299–303 (2004).
5. Sun, S. J., Tian, Y. Z., Lin, H. R., Wang, Z. J. & Zhang, Z. F. Revisiting the role of prestrain history in the mechanical properties of ultrafine-grained CoCrFeMnNi high-entropy alloy. *Mater. Sci. Eng.: A* **801**, 140398 (2021).
6. Wang, Y., Zhang, M., Jin, J., Gong, P. & Wang, X. Oxidation behavior of CoCr-FeMnNi high entropy alloy after plastic deformation. *Corros. Sci.* **163**, 108285 (2020).
7. Wang, Y. et al. Effect of the grain size on the corrosion behavior of CoCrFeMnNi HEAs in a 0.5 M H$_2$SO$_4$ solution. *J. Alloy. Compd.* **858**, 157712 (2020).
8. Ma, L., Wang, L., Zhang, T. & Inoue, A. Bulk glass formation of Ti-Zr-Hf-Cu-M (M = Fe, Co, Ni) alloys. *Mater. Trans.* **43**, 277–280 (2002).
9. Gao, X. Q. et al. High mixing entropy bulk metallic glasses. *J. Non-Cryst. Solids* **357**, 3557–3560 (2011).
10. Wang, W. H. High-entropy metallic glasses. *JOM* **66**, 2067–2077 (2014).
11. Gong, P. et al. Influence of deep cryogenic cycling on the rejuvenation and plasticization of TiZrHfBeCu high-entropy bulk metallic glass. *Mater. Sci. Eng.: A* **797**, 140078 (2020).
12. Ding, H. Y. & Yao, K. F. High entropy $Ti_{20}Zr_{20}Cu_{20}Ni_{20}Be_{20}$ bulk metallic glass. *J. Non-Cryst. Solids* **364**, 9–12 (2013).
13. Ding, H. Y., Shao, Y., Gong, P., Li, J. F. & Yao, K. F. A senary TiZrHfCuNiBe high entropy bulk metallic glass with large glass-forming ability. *Mater. Lett.* **125**, 151–153 (2014).
14. Zhao, S. F., Yang, G. N., Ding, H. Y. & Yao, K. F. A quinary Ti-Zr-Hf-Be-Cu high entropy bulk metallic glass with a critical size of 12 mm. *Intermetallics* **61**, 47–50 (2015).
15. Zhao, S. F. et al. Pseudo-quinary $Ti_{20}Zr_{20}Hf_{20}Be_{20}(Cu_{20−x}Ni_x)$ high entropy bulk metallic glasses with large glass forming ability. *Mater. Des.* **87**, 625–631 (2015).
16. Huo, J. et al. The magnetocaloric effect of Gd-Tb-Dy-Al-M (M = Fe, Co and Ni) high-entropy bulk metallic glasses. *Intermetallics* **58**, 31–35 (2015).
17. Li, J. et al. Distinct spin glass behavior and excellent magnetocaloric effect in $Er_{20}Dy_{20}Co_{20}Al_{20}Re_{20}$ (Re = Gd, Tb and Tm) high-entropy bulk metallic glasses. *Intermetallics* **96**, 90–93 (2018).

18. Li, C. et al. New ferromagnetic $(Fe_{1/3}Co_{1/3}Ni_{1/3})_{80}(P_{1/2}B_{1/2})_{20}$ high entropy bulk metallic glass with superior magnetic and mechanical properties. *J. Alloy. Compd.* **791**, 947–951 (2019).

19. Takeuchi, A. et al. $Pd_{20}Pt_{20}Cu_{20}Ni_{20}P_{20}$ high-entropy alloy as a bulk metallic glass in the centimeter. *Intermetallics* **19**, 1546–1554 (2011).

20. Xu, Y., Li, Y., Zhu, Z. & Zhang, W. Formation and properties of $Fe_{25}Co_{25}Ni_{25}(P, C, B, Si)_{25}$ high-entropy bulk metallic glasses. *J. Non-Cryst. Solids* **487**, 60–64 (2018).

21. Li, Y., Zhang, W. & Qi, T. New soft magnetic $Fe_{25}Co_{25}Ni_{25}(P, C, B)_{25}$ high entropy bulk metallic glasses with large supercooled liquid region. *J. Alloy. Compd.* **693**, 25–31 (2017).

22. Qi, T. et al. Soft magnetic $Fe_{25}Co_{25}Ni_{25}(B, Si)_{25}$ high entropy bulk metallic glasses. *Intermetallics* **66**, 8–12 (2015).

23. Jin, X. et al. CoCrFeMnNi high-entropy alloy powder with excellent corrosion resistance and soft magnetic property prepared by gas atomization method. *Materwiss. Werksttech.* **50**, 837–843 (2019).

24. Rogal, A., Kalita, D., Tarasek, A., Bobrowski, P. & Czerwinski, F. Effect of SiC nano-particles on microstructure and mechanical properties of the CoCrFeMnNi high entropy alloy. *J. Alloy. Compd.* **708**, 344–352 (2017).

25. Kim, J. et al. Utilization of high entropy alloy characteristics in Er-Gd-Y-Al-Co high entropy bulk metallic glass. *Acta Mater.* **155**, 350–361 (2018).

26. Wang, Y. B. et al. Biodegradable CaMgZn bulk metallic glass for potential skeletal application. *Acta Biomater.* **7**, 3196–3208 (2011).

27. Gong, P. et al. Room temperature nanoindentation creep behavior of TiZrHfBe-Cu(Ni) high entropy bulk metallic glasses. *Mater. Sci. Eng.: A* **688**, 174–179 (2017).

28. Liens, A. et al. Effect of alloying elements on the microstructure and corrosion behavior of TiZr-based bulk metallic glasses. *Corros. Sci.* **177**, 108854 (2020).

29. Coimbrão, D. D. et al. Corrosion properties of amorphous, partially, and fully crystallized $Fe_{68}Cr_8Mo_4Nb_4B_{16}$ alloy. *J. Alloy. Compd.* **826**, 154123 (2020).

30. Luo, H. et al. Influence of carbon on the corrosion behaviour of interstitial equiatomic CoCrFeMnNi high-entropy alloys in a chlorinated concrete solution. *Corros. Sci.* **163**, 108287 (2020).

31. Shi, Y. et al. Homogenization of al CoCrFeNi high-entropy alloys with improved corrosion resistance. *Corros. Sci.* **133**, 120–131 (2018).

32. Li, Y. et al. New FeNiCrMo(P, C, B) high-entropy bulk metallic glasses with unusual thermal stability and corrosion resistance. *J. Mater. Sci. Technol.* **43**, 32–39 (2020).

33. Peker, A. & Johnson, W. L. A highly processable metallic glass: $Zr_{41.2}Ti_{13.8}Cu_{12.5}Ni_{10.0}Be_{22.5}$. *Appl. Phys. Lett.* **63**, 2342–2344 (1993).

34. Guo, S., Hu, Q., Ng, C. & Liu, C. T. More than entropy in high-entropy alloys: forming solid solutions or amorphous phase. *Intermetallics* **41**, 96–103 (2013).

35. Tang, J. et al. Effect of atomic mobility on the electrochemical properties of a $Zr_{58}Nb_3Cu_{16}Ni_{13}Al_{10}$ bulk metallic glass. *Electrochim. Acta* **267**, 222–233 (2018).

36. Pelletier, J. M. Influence of structural relaxation on atomic mobility in a $Zr_{41.2}Ti_{13.8}Cu_{12.5}Ni_{10.0}Be_{22.5}$ (Vit1) bulk metallic glass. *J. Non-Cryst. Solids* **354**, 3666–3670 (2008).

37. Qiao, J. C., Pelletier, J. M., Kou, H. C. & Zhou, X. Modification of atomic mobility in a Ti-based bulk metallic glass by plastic deformation or thermal annealing. *Intermetallics* **28**, 128–137 (2012).

38. Fabas, A. et al. Metal dusting corrosion of austenitic alloys at low and high pressure with the effects of Cr, Al, Nb and Cu. *Corros. Sci.* **123**, 310–318 (2017).

39. Xu, Z. et al. Corrosion resistance enhancement of CoCrFeMnNi high-entropy alloy fabricated by additive manufacturing. *Corros. Sci.* **177**, 108954 (2020).

40. Brug, G. J., van den Eeden, A. L. G., Sluyters-Rehbach, M. & Sluyters, J. H. The analysis of electrode impedances complicated by the presence of a constant phase element. *J. Electroanal. Chem. Interfacial Electrochem.* **176**, 275–295 (1984).

41. Hsu, C. H. & Mansfeld, F. Technical note: concerning the conversion of the constant phase element parameter Y_0 into a capacitance. *Corrosion* **57**, 747–748 (2001).

42. Ogle, K., Mokaddem, M. & Volovitch, P. Atomic emission spectroelectrochemistry applied to dealloying phenomena ii. Selective dissolution of iron and chromium during active-passive cycles of an austenitic stainless steel. *Electrochim. Acta* **55**, 913–921 (2010).

43. Dutta, G., Siddiqui, S., Zeng, H., Carlisle, J. A. & Arumugam, P. U. The effect of electrode size and surface heterogeneity on electrochemical properties of ultrananocrystalline diamond microelectrode. *J. Electroanal. Chem.* **756**, 61–68 (2015).

44. Gan, Z., Zhang, C., Zhang, Z., Chen, Z. & Liu, L. Crystallization-dependent transition of corrosion resistance of an Fe-based bulk metallic glass under hydrostatic pressures. *Corros. Sci.* **179**, 109098 (2021).

45. Li, Z., Zhang, C. & Liu, L. Wear behavior and corrosion properties of Fe-based thin film metallic glasses. *J. Alloy. Compd.* **650**, 127–135 (2015).

46. Shuang, S., Ding, Z. Y., Chung, D., Shi, S. Q. & Yang, Y. Corrosion resistant nanostructured eutectic high entropy alloy. *Corros. Sci.* **164**, 108315 (2020).

47. Hamadou, L., Kadri, A. & Benbrahim, N. Characterisation of passive films formed on low carbon steel in borate buffer solution (pH 9.2) by electrochemical impedance spectroscopy. *Appl. Surf. Sci.* **252**, 1510–1519 (2005).

48. Zhang, L. M. et al. Thermally induced structure evolution on the corrosion behavior of Al-Ni-Y amorphous alloys. *Corros. Sci.* **144**, 172–183 (2018).

49. Gu, J., Shao, Y., Bu, H., Jia, J. & Yao, K. An abnormal correlation between electron work function and corrosion resistance in Ti-Zr-Be-(Ni/Fe) metallic glasses. *Corros. Sci.* **165**, 108392 (2020).

50. Zhou, Y. & Niinomi, M. Passive films and corrosion resistance of Ti-Hf alloys in 5% HCl solution. *Surf. Coat. Technol.* **204**, 180–186 (2009).

51. Hu, Y., Huang, S., Liu, S. & Pan, W. A corrosion-resistance super-hydrophobic TiO_2 film. *Appl. Surf. Sci.* **258**, 7460–7464 (2012).

52. Pourbaix, M. Atlas of electrochemical equilibria in aqueous solution. *J. Electroanal. Chem* **13**, 471 (1967).

53. Gu, J., Lu, S., Shao, Y. & Yao, K. Segregating the homogeneous passive film and understanding the passivation mechanism of Ti-based metallic glasses. *Corros. Sci.* **178**, 109078 (2021).

54. Bojinov, M. et al. The mechanism of transpassive dissolution of Ni-Cr alloys in sulphate solutions. *Electrochim. Acta* **45**, 2791–2802 (2000).

55. Macdonald, D. D. The history of the point defect model for the passive state: a brief review of film growth aspects. *Electrochim. Acta* **56**, 1761–1772 (2011).

56. Macdonald, D. D. The point defect model for the passive state. *J. Electrochem. Soc.* **139**, 3434–3449 (1992).

57. Li, Y. & Xu, J. Differences in pitting growth kinetics between $Zr_{60}Ni_{25}Al_{15}$ and $Zr_{60}Cu_{25}Al_{15}$ metallic glasses exposed to a 0.6 M NaCl aqueous solution. *Corros. Sci.* **128**, 73–84 (2017).

58. Gu, J., Shao, Y., Shi, L., Si, J. & Yao, K. Novel corrosion behaviours of the annealing and cryogenic thermal cycling it treated Ti-based metallic glasses. *Intermetallics* **110**, 106467 (2019).

59. Green, B. A. et al. A study of the corrosion behaviour of $Zr_{50}Cu_{40-x}Al_{10}Pd_x$ bulk metallic glasses with scanning auger microanalysis. *Corros. Sci.* **50**, 1825–1832 (2008).

60. Kamachi Mudali, U., Baunack, S., Eckert, J., Schultz, L. & Gebert, A. Pitting corrosion of bulk glass-forming zirconium-based alloys. *J. Alloy. Compd.* **377**, 290–297 (2004).

61. Jayaraj, J., Gebert, A. & Schultz, L. Passivation behaviour of structurally relaxed $Zr_{48}Cu_{36}Ag_8Al_8$ metallic glass. *J. Alloy. Compd.* **479**, 257–261 (2009).

62. Ding, J. et al. High entropy effect on structure and properties of (Fe, Co, Ni, Cr)-B amorphous alloys. *J. Alloy. Compd.* **696**, 345–352 (2017).

63. Yeh, J. Alloy design strategies and future trends in high-entropy alloys. *JOM* **65**, 1759–1771 (2013).

64. Ranganathan, S. Alloyed pleasures: multimetallic cocktails. *Curr. Sci.* **85**, 1404–1406 (2003).

ACKNOWLEDGEMENTS

AUTHOR CONTRIBUTIONS

P.G. designed the experiments, analyzed the results, and wrote the paper. D.L.W., C.Z., and Y.W. contributed to the experiments of the DSC, XRD, DMA, SEM, XPS, TEM, and its data processing. Z.J.-S., M.Z., K.F.Y., and X.Y.W. revised the paper. All the authors contributed to the interpretation of the experimental data.

COMPETING INTERESTS

The authors declare no competing interests.

ADDITIONAL INFORMATION

Correspondence and requests for materials should be addressed to Pan Gong or Xinyun Wang.

Reprints and permission information is available at http://www.nature.com/reprints

Publisher's note Springer Nature remains neutral with regard to jurisdictional claims in published maps and institutional affiliations.